

All-fiber ultrafast image detection enabled by deep learning

Zhoutian Liu

Tsinghua University

Lele Wang

Tsinghua University

Yuan Meng

Tsinghua University

Tiantian He

Tsinghua University

Sifeng He

Tsinghua University

Yousi Yang

Tsinghua University

Liuyue Wang

Tsinghua University

Jiading Tian

Tsinghua University <https://orcid.org/0000-0002-6764-1086>

Dan Li

Tsinghua University

Ping Yan

Tsinghua University <https://orcid.org/0000-0002-8177-7019>

Mali Gong

Tsinghua University

Qiang Liu

Tsinghua University

Qirong Xiao (✉ xiaoqirong@mail.tsinghua.edu.cn)

Tsinghua University <https://orcid.org/0000-0001-9419-3939>

Article

Keywords: image detection, deep learning, engineering, chemistry, material science, biomedicine

Posted Date: June 17th, 2021

DOI: <https://doi.org/10.21203/rs.3.rs-568362/v1>

License:  This work is licensed under a Creative Commons Attribution 4.0 International License.

[Read Full License](#)

Version of Record: A version of this preprint was published at Nature Communications on March 17th, 2022. See the published version at <https://doi.org/10.1038/s41467-022-29178-8>.

All-fiber ultrafast image detection enabled by deep learning

Abstract: Detection of dynamical scenes at ultrafast speeds serves as a foundation for modern engineering, chemistry, material science and biomedicine, et al. For biomedical applications, in vivo microscopic imaging is often required, which has led to the development of fiber-probe-based endoscopy. However, the combination of ultrafast image acquiring with fiber endoscopy has not yet been achieved, which is vital for exploration of transient biomedical phenomena. Here, we propose a scheme of all-fiber image detection at an ultrafast speed without any free-space optical elements. Image detection is achieved based on the transformation of two-dimensional spatial information into one-dimensional temporal pulsed signal streams by leveraging the high intermodal dispersion in a multimode fiber. Deep learning algorithms are subsequently deployed to reconstruct the images detected by the fiber probe from the temporal waveforms acquired at the other end of the fiber. The fiber probe can directly detect micron-scale objects without any bulk objective, and image detection has been experimentally realized with a high frame rate (15 Mfps), a large frame depth (10^4) and extremely short shutter time (30 ps) simultaneously. This ultrafast detection scheme, combined with high mechanical flexibility and high level of integration, can stimulate future research on exploring various in-vivo ultrafast phenomena.

Introduction

Ultrafast image detection is vital for observing microscopic and transient physical phenomena¹. To date, silicon-based imaging sensors, charge-coupled device (CCD) or complementary metal-oxide-semiconductor (CMOS) cameras, have achieved imaging speeds of up to millions of frames per second (fps)². Some advanced systems are also invented for even faster transient imaging, reaching trillions of fps, including sequentially timed all-optical mapping photography (STAMP)³, frequency-domain tomography⁴, femtosecond time-resolved optical polarimetry⁵, and compressed ultrafast spectral photography⁶. These advanced technologies have helped researchers better understand various transient phenomena, such as lattice dynamics⁷, hot-electron diffusion⁸, evolution of laser ablation⁹ and production of electronic plasmas¹⁰. However, in some other fields, especially in vivo applications¹¹, ultrafast detection requires new technologies for imaging in such narrow spaces, for which emerging fiber-based detection technology has unique advantages.

In contrast to bulk imaging systems, fiber-based imaging systems feature high mechanical flexibility, compact sizes and resistance to ambient interference. These features have made fiber-based imaging a competitive candidate for detecting images under special circumstances, for example, in environments with high temperatures, pressures or radiation levels. Fiber probes can also penetrate deep into narrow spaces for endoscopy, which is essential in fields such as biomedicine¹² and microfluidics¹³. Fiber endoscopy with a high frame rate is especially necessary in some special scenarios. For instance, a fiber probe can be inserted into the cerebral cortex to examine the fast signals of neural activation¹⁴ or used in vivo to observe chemical dynamics in living tissues¹⁵. In physics and engineering, such probes can also be used for observing ultrafast physical reactions in closed containers¹⁶ or exploring the fuel injection dynamics in internal combustion engines.

However, for currently prevalent fiber-based imaging systems, their ability to ultrafast detection is

44 limited by the CCD or CMOS cameras that serve as essential parts in their systems. The basic
45 principle of these technologies is to analyze the light fields at the output fiber facet and reconstruct
46 the 2D images using such as transmission matrix methods and deep learning methods^{14,17}. Due to
47 such a principle, they must detect the fields of different frames at a fixed position, which means that
48 they can only use conventional single-sensor cameras (special cameras such as rotating-mirror
49 cameras¹⁸ and framing cameras that have higher frame rates are inapplicable). While the single
50 imaging sensor faces the challenge of slow readout process from the pixel arrays to the memory¹⁹,
51 both the frame rate, frame depth (number of frames that can be captured in a single shot) and shutter
52 time (exposure time of one frame) of those fiber-based imaging systems are limited. To the best of
53 our knowledge, the world's fastest single-sensor camera has a frame rate of 10 Mfps, a frame depth
54 of 256 frames and shutter time of 50 ns (see [https://www.shimadzu.com/an/products/materials-
55 testing/high-speed-video-camera/hyper-vision-hpv-x2/index.html](https://www.shimadzu.com/an/products/materials-testing/high-speed-video-camera/hyper-vision-hpv-x2/index.html)), which puts an upper limit on
56 these systems. In addition, free-space optical elements are also commonly needed in collection of
57 the output fields, which reduce the level of integration and make those systems susceptible to
58 environmental disturbances.

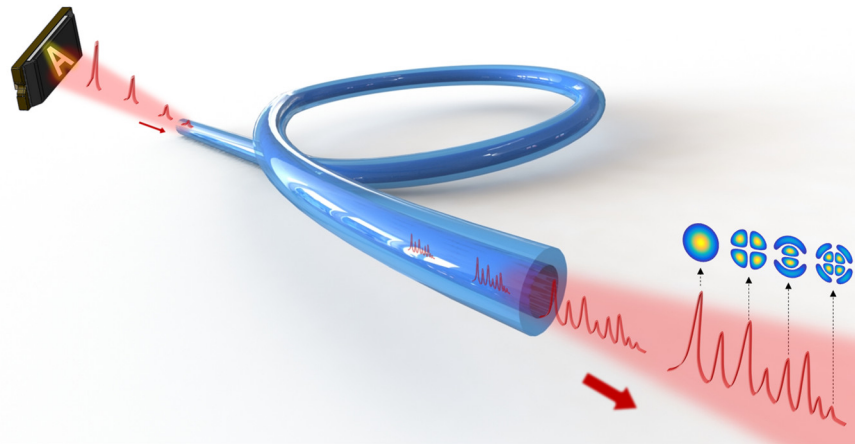
59
60 Fortunately, a time-stretching imaging method (or serial time-encoded amplified microscopy,
61 abbreviated as STEAM)²⁰⁻²² has been proposed to eliminate these pixelated sensors by encoding the
62 spatial information of objects into time-domain signals, which requires only a one-pixel detector.
63 Since each optical pulse can carry the information of one image frame, a high frame rate can be
64 achieved by recording the temporal signals of a pulse train with a high repetition rate. However,
65 such systems require bulk spatial dispersers, which are not compatible with the fiber endoscopy.

66
67 To combine the advantages of the time-stretching method and the fiber endoscopy, we propose a
68 novel method to enable all-fiber ultrafast detection of images. Using a single multimode fiber (MMF)
69 as the probe, real-time image acquisition with a frame rate of over 15 Mfps and a shutter time of
70 approximately 30 ps is experimentally demonstrated, in which 10,000 frames can be recorded in a
71 single shot. Leveraging the intermodal dispersion effect in an MMF, we transform two-dimensional
72 (2D) spatial information into one-dimensional (1D) time-domain pulsed waveforms. A U-Net neural
73 network model is trained to reconstruct the images from the temporal waveforms recorded by an
74 ultrafast photodiode connected to the output end of the fiber. In addition, we propose an all-fiber
75 structure for the first time by combining a fiber-output pulse laser, a triple-cladding fiber probe and
76 a side-pump coupler. Such a scheme enables unprecedentedly high levels of integration and system
77 stability.

78 79 **Results**

80 **Principles.** The light fields in an MMF can be resolved into a set of orthogonal spatial modes²³ that
81 enable the transmission of spatial information. It has been verified that the information of images
82 with $4N$ resolvable features can be carried in a single MMF, where N is the number of spatial modes
83 per polarization²⁴. When light scattered by an object is collected by an MMF, various fiber modes
84 will be excited to different degrees. When we use an ultrafast pulse laser as the illumination source,
85 the energy of each pulse entering the MMF can be dispersed into different modes. Because the
86 different modes have different group velocities, the pulses in these modes will arrive at the other
87 end of the MMF with different time delays. If the intermodal dispersion of the MMF is sufficiently

88 large, after transmission through the MMF, a pulse with a temporal duration of less than the delay
89 difference between two modes will be split into a number of isolated subpulses in the time domain,
90 as schematically shown in Fig. 1. If the power of the pulse is sufficiently low and its wavelength
91 bandwidth is sufficiently narrow, both the chromatic dispersion and nonlinear effects in the MMF
92 can be ignored, resulting in the pulse evolution being dominated by the intermodal dispersion^{25,26}
93 (see Supplementary Note 1 for details). Therefore, the temporal distribution of the train of subpulses
94 will depend on the mode composition of the original pulse, which is determined by the spatial
95 distribution of the object. Hence, the spatial information of objects can be encoded into the time
96 waveforms of the output pulses.



97

98 Fig. 1 The evolution of ultrashort pulses in a long MMF with large intermodal dispersion.

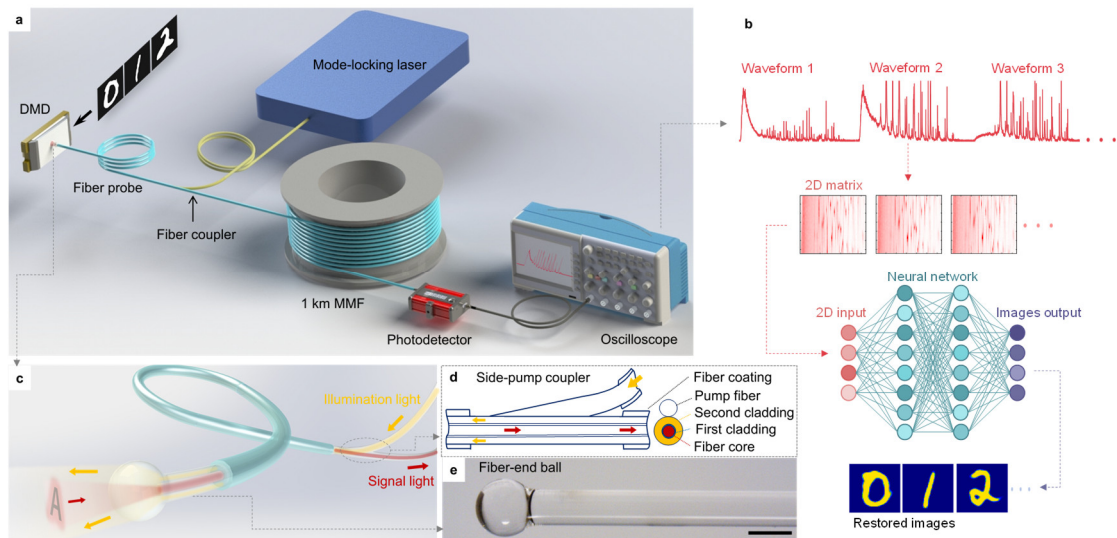
99

100 **Experimental setup.** The structure of the system is illustrated in Fig. 2(a). The illumination pulses
101 from a mode-locked fiber laser are directly coupled into the fiber probe by a side-pump coupler²⁷.
102 After approximately 2 meters of transmission, the illumination pulses emerge from the fiber probe
103 to illuminate the intensity patterns displayed by a digital micromirror device (DMD). Then, the light
104 reflected from the patterns reenters the fiber probe, as shown in Fig. 2(c). Thus, the illumination and
105 reception of light are integrated into a single fiber probe. The other end of the fiber probe is spliced
106 with a 1-km MMF (50/125 μm and numerical aperture (NA) = 0.22), in which the spatial
107 information carried in the signal pulses is transformed into temporal waveforms. This length
108 guarantees that the delay differences between different modes are sufficiently large to cause each a
109 signal pulse to split into a burst of subpulses. The temporal waveforms of the pulses at the other end
110 of the MMF are detected by an ultrafast photodetector and stored into the memory of an oscilloscope
111 instantly. In the training stage, different displayed images and the corresponding waveforms are
112 used to train the neural network model. After training, the network is capable of recovering new
113 images directly from the acquired waveforms, as shown in Fig. 2(b).

114

115 The fiber probe is a triple-cladding fiber, and both the core and the second cladding layer can
116 transmit light. The structure of the side-pump coupler, where the illumination light is coupled into
117 the second cladding layer of the fiber probe (see Supplementary Note 2 for the detailed structure),
118 is schematically shown in Fig. 2(d). Although the light reflected by the DMD will enter both the
119 core and cladding of the fiber probe, only the light in the core (signal light) can enter the MMF due
120 to the NA and diameter match between the fiber probe core and the MMF core. The end of the fiber
121 probe is fused into a microball with a 580 μm diameter, as shown in Fig. 2(e), which serves to

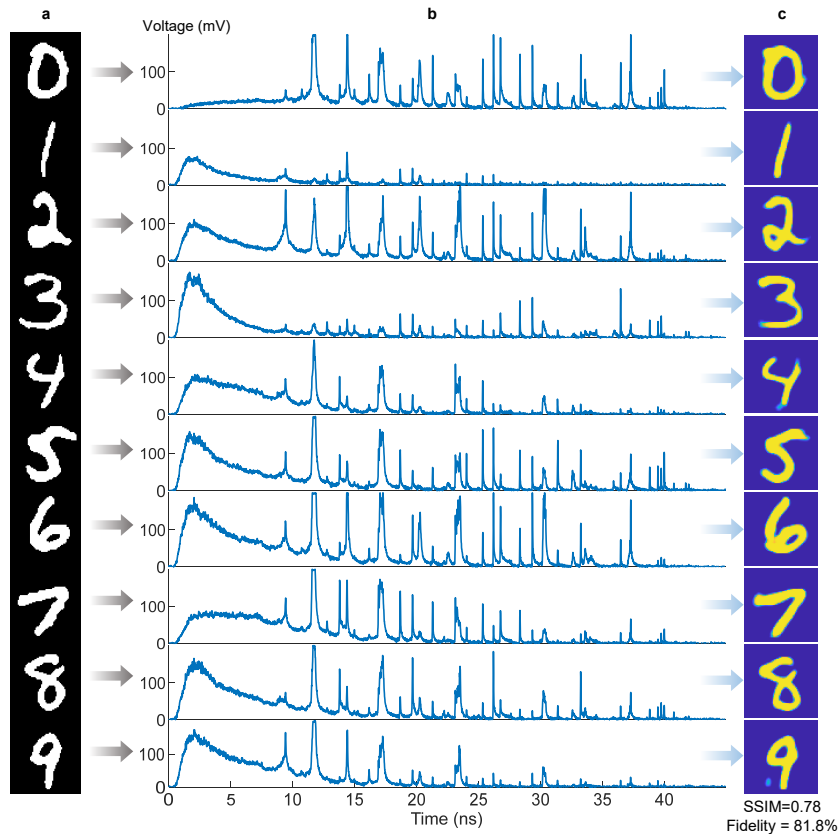
122 produce more uniform and focused illumination (in the absence of this microball, the beam
 123 emerging from the cladding of the fiber would have an annular shape). This probe can be directly
 124 moved very close to microscale objects for imaging, with no requirement of objectives that are vital
 125 for conventional cameras. To demonstrate this, the fiber-end ball probe was placed very close to the
 126 surface of the DMD, such that it could receive only light returning from a very small part of the
 127 DMD. This small region was measured to have an area of approximately $200 \times 200 \mu\text{m}^2$, in which
 128 images of approximately 28×28 pixels can be displayed.



129
 130 Fig. 2 (a) Schematic of the experimental setup. (b) Flow of the reconstruction process from waveforms to images.
 131 (c) Schematic of the fiber-end ball and the side-pump fiber coupler and the flow of illumination light and signal light.
 132 (d) Structure of the side-pump coupler and the triple-cladding fiber probe, where the illumination light is coupled
 133 into and transmitted in the cladding of the fiber, while the signal light is collected and transmitted in the fiber core
 134 in the opposite direction. (e) A micrograph of the fiber-end ball. Scale bar: $500 \mu\text{m}$.

135
 136 **Image recovery.** Fig. 3(a) and 3(b) show several example images from the MNIST dataset²⁸ and
 137 their corresponding temporal waveforms. We see that after transmission through the long MMF, a
 138 27.5-ps input pulse splits into a burst of subpulses over approximately 45 ns (see Supplementary
 139 Note 3 for more waveform details). A U-Net model was trained on 19000 waveform/image pairs to
 140 learn the mapping (the training details are described in the Methods section). Using the trained
 141 model, we could directly recover other new images from the corresponding acquired waveforms.
 142 The recovery results corresponding to these example images are shown in Fig. 3(c). The results for
 143 1000 test images show an average fidelity (calculated as the 2D correlation) of 81.8% and average
 144 structural similarity index measure (SSIM, which correlates well with human perception) of 0.78.
 145 Compared with previous fiber endoscopy technologies, which generally operate at low frame
 146 rates^{17,29,30}, our scheme shows comparable performance in terms of image quality.

147



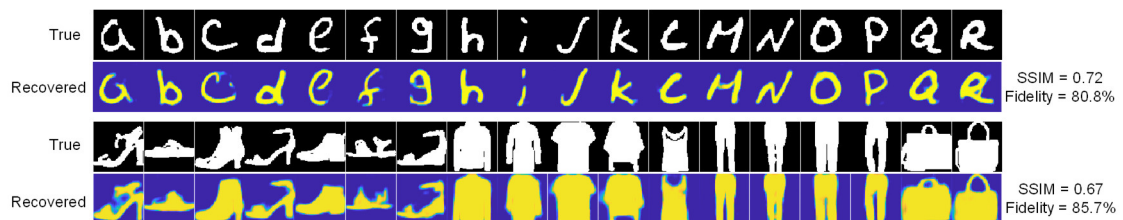
148

149 Fig. 3 (a) Example images of digits 0 – 9 selected from the test database and (b) their corresponding output
 150 waveforms. (c) Images recovered from the waveforms.

151

152 We also tested the reconstruction performance for several different types of images, including
 153 handwritten letters from the EMNIST dataset³¹ and patterns of clothes from the Fashion-MNIST
 154 dataset³². After a similar training process, the images could be recovered, and some examples are
 155 shown in Fig. 4, along with the average fidelity and SSIM. The results show the high practicability
 156 of our scheme. While the waveform corresponding to one pulse corresponds to one image,
 157 successive pulses can enable the detection of images at a frame rate of 15 Mfps, consistent with the
 158 repetition rate of the pulse source. Moreover, the shutter time is only approximately 30 ps, which is
 159 equal to the time duration of one pulse.

160



161

162 Fig. 4 Some example images of letters and clothes and the retrieved images.

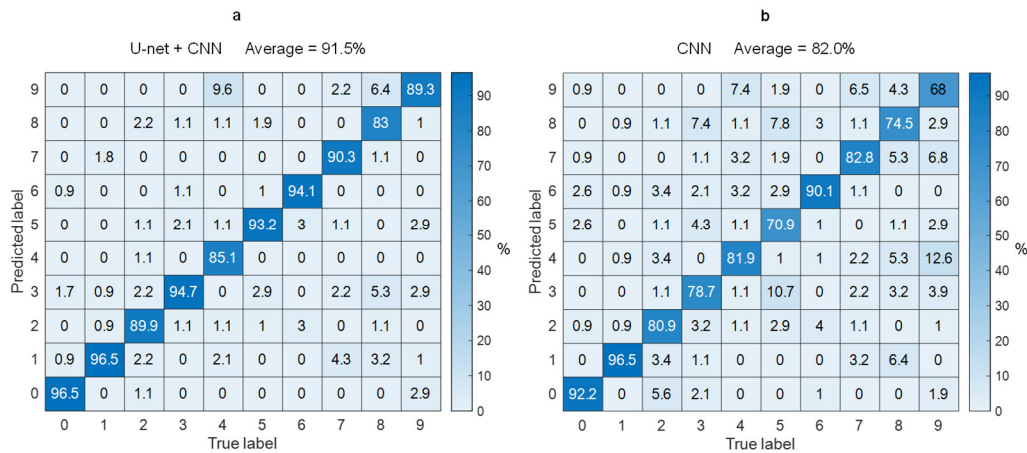
163

164 Finally, we verified that instead of utilizing the waveforms with the highest sampling rate (10 ps⁻¹)
 165 recorded by the oscilloscope, when the waveforms are down sampled to a small number of feature
 166 points, the images can still be recovered at the cost of a slight reduction in imaging quality (see

167 Supplementary Note 5). We down sampled the waveforms to only 256 points, which were then fed
 168 to the network. The results for the test images of handwritten digits show an average fidelity and
 169 SSIM of 77.2% and 0.73, respectively. These findings indicate that the main information is encoded
 170 only in certain feature points of the waveforms. This property can help to reduce the requirements
 171 of the sampling circuits and improve the signal processing speed in real applications.

172

173 **Image classification.** This system can also be used for high-speed classification, which has great
 174 value in fields such as biomedicine and microfluidics¹³. Here, we demonstrate the classification of
 175 handwritten digits based on the acquired waveforms. We use a single convolutional neural network
 176 (CNN) to learn the classification while either the retrieved images output from the U-Net or the
 177 original waveforms data are used as the input of network (see Supplementary Note 4 for details). In
 178 testing on 1000 new images, a high accuracy of 91.5% was achieved as indicated by Fig. 5,
 179 indicating that the combination of the U-Net and CNN can exhibit a higher accuracy. We note that
 180 image detection through such long fibers has been a major challenge for conventional multimode
 181 imaging systems³⁰ because the disturbance grows more severe as the fiber length increases²⁹,
 182 making the recovery more difficult (the accuracy dropped to less than 70% for a 1-km MMF in a
 183 previous research). However, in our scheme, the classification accuracy remains at such a high level
 184 under the same length, showing high interference immunity and practicability. This superiority can
 185 probably be attributed to low crosstalk between different modes, when the pulse energy in them has
 186 been separated after transmission over a certain distance in the MMF, thus, the energy coupling
 187 between different modes is suppressed. Such a feature makes our scheme also well suitable for long-
 188 distance detection.



189

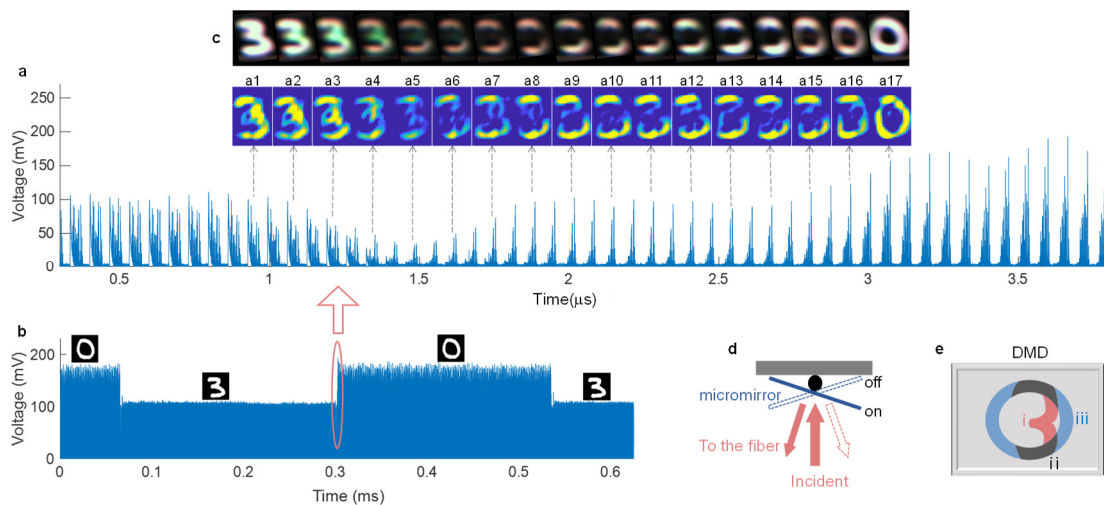
190 Fig. 5 Confusion matrixes for the classification of 1000 test images using (a) a combined U-Net and CNN model
 191 and (b) the CNN alone. These matrixes present the statistics of what proportion of each digit is correctly classified.
 192 Each matrix element gives the possibility of instances in which one number (true label) is recognized as another
 193 number (predicted label).

194

195

196 **Ultrafast detection.** To verify the feasibility of ultrafast detection, we adjusted the time scale of the
 197 oscilloscope to the maximum (650 μ s) so that it would store approximately 10,000 waveforms in a
 198 single record. Although the highest refresh rate of the DMD used here is limited to 4.3 kHz,
 199 preventing it from displaying an ultrafast video that matches our detection frame rate of 15 Mfps,

200 the refresh processes when the DMD switches from one image to another are nearly transient and
 201 occur within $3\ \mu\text{s}$ (see the recorded waveforms below). Thus, we chose to detect such a refresh
 202 process using our system to reveal the detailed refresh process in such a short time. We set the DMD
 203 to periodically display two images and simultaneously record the time signals, as shown in Fig. 6(b).
 204 The detailed waveforms corresponding to one refresh process (marked with a red circle) are shown
 205 in Fig. 6(a), where we can see the process of the waveform corresponding to an image “3” gradually
 206 changing to the waveform corresponding to an image “0” within $3\ \mu\text{s}$. The retrieved successive
 207 frames are shown in the insets (a1 – a17), from which we can understand the refresh process of the
 208 DMD. The whole refresh process can be divided into 3 stages. In stage 1 (insets a1 – a5), the DMD
 209 initially displays the “3” image, which means that the micromirrors in regions (i) and (ii) of the
 210 DMD (see Fig. 6e) are in the “on” state, while the others are in the “off” state. The states of the
 211 micromirrors are explained in Fig. 6(d), where region (ii) represents the overlap between the “0”
 212 and “3” images. When the DMD starts to refresh to “0” image, the micromirrors in regions (i) and
 213 (iii) rotate to the opposite directions³³, causing the light in region (i) to fade away. In stage 2 (insets
 214 a6 - a14), only the light from region (ii) can be observed because the micromirrors there will hold
 215 the states of “on”. In stage 3 (insets a15 - a17), the light from region (iii) appears, indicating that the
 216 corresponding micromirrors have rotated into the “on” state. Thus, the image “3” has been refreshed
 217 to the image “0”. For comparison, we also used a high-speed camera to record the refresh process
 218 (see the Methods section for details), and the real images captured are shown in Fig. 6(c). We can
 219 see that the change in the patterns is consistent with what we have observed using our system.
 220



221
 222 Fig. 6 (a) The waveforms collected during the transient time when the DMD refreshes from an image “3” to an image
 223 “0”. Insets (a1 - a17) show the images reconstructed from some of these waveforms. (b) The waveforms recorded
 224 with the DMD periodically displaying two images, from which we see that each image has an exposure time of $235\ \mu\text{s}$,
 225 which is spent by the DMD in loading the data for the next image into the memory cells beneath its pixels. After
 226 all the data have been loaded, the DMD switches to the other image within only $3\ \mu\text{s}$, as marked by the red circle.
 227 (c) The real images of the DMD captured during the refresh process using a high-speed camera. (d) Structure of one
 228 pixel of the DMD. A DMD chip has many micromirrors on its surface, which correspond to the pixels in the image
 229 to be displayed. These micromirrors can be individually rotated by approximately $\pm 12^\circ$ to an “on” or “off” state. In
 230 the “on” state, the illumination light is reflected back to the fiber probe. In the “off” state, the light is directed in
 231 another direction. Thus, the array of micromirrors can produce intensity modulations on the light field. When the

232 DMD refreshes its current image, all micromirrors move to their assigned states at the same moment. (e) Schematic
233 of the patterns of the digits “3” and “0” displayed on the DMD chip. When the DMD switches from “3” to “0”, the
234 micromirrors in the overlapping region of the two images (region ii) do not change their states, while those in regions
235 (i) and (iii) rotate to the opposite directions.

237 Discussion

238 Because the proposed scheme needs only a single photodiode rather than pixelated sensors, it can
239 be easily applied to other wavelengths. For example, considering that the InGaAs-based photodiode
240 used here has a high sensitivity over a broad wavelength band from 1 μm to 1.6 μm ³⁴, while the
241 silica fiber has very low attenuation in this band, our scheme can be easily extended to other
242 wavelengths in this band. This will be of great help in real applications because conventional Si-
243 based CCD and CMOS cameras are sensitive only to wavelengths below 1.1 μm ¹⁹. Our method also
244 has the potential to operate in the mid-infrared and THz bands considering the maturity of
245 photodetectors in these bands. In addition, in the mid-infrared, the use of a fluoride-glass fiber can
246 significantly reduce the optical loss, while in the THz band, much work has focused on the
247 development of waveguides with reduced loss and dispersion³⁵, which make it possible to develop
248 long waveguides with high intermodal dispersion in these bands. Thus, we may apply the same
249 principle to these bands. This will be helpful for detecting certain materials that have a strong
250 response only at these wavelengths or for detection under special conditions in which only light in
251 these bands can be transmitted with low loss. Summing up the above, our scheme can offer a new
252 approach for observing vivid physical phenomena in a vast number of scenarios.

254 The performance of our demonstrated proof-of-principle system may be further improved. The
255 wavelength of the source used here (1064 nm) is much longer than those adopted in most previous
256 studies^{17,23,29,30}, which will result in a much smaller number of excited modes and, thus, much less
257 spatial information carried in the MMF. Hence, by using an MMF with a larger core and higher NA,
258 more spatial information can be collected, and the resolution of the images that can be recovered
259 will, in theory, be much higher. In addition, the shutter time can be made even shorter to enable the
260 detection of faster events by using shorter pulses. More importantly, if one splices a fiber amplifier
261 to the end of the MMF, the pulse signals can be significantly amplified, which will greatly enhance
262 the sensitivity of the detection system to make it suitable for detecting very weak signals. Moreover,
263 because the illumination zone and intensity are limited for this fiber probe, the current system is
264 suitable only for detecting small objects. If one wishes to detect a larger object, an objective can be
265 used in front of the fiber probe to couple more light from the object into the probe. Additionally, if
266 one wishes to use a brighter illumination, an auxiliary illumination can be adopted at the cost of
267 reducing the systems' level of integration, as discussed in Supplementary Note 6.

269 Our scheme can be further modified to detect 3D objects by combining it with the existing time-of-
270 flight technique³⁶⁻³⁸, in which ultrafast pulses are generally applied to illuminate the objects of
271 interest and an ultrafast camera is used to detect the reflected light at different arrival times. Because
272 light reflected from different depths on the object will arrive at the camera with different time delays,
273 the variations in the 2D images captured over time can reveal the 3D information of the object. The
274 system we present here is naturally compatible with the time-of-flight method because we also adopt
275 an ultrafast pulse laser for illumination. If we use the fiber probe to detect a 3D object, the temporal

276 waveforms will contain both depth information and 2D spatial information. Thus, through specific
277 reconstruction algorithms, it will be possible to recover the 3D information encoded in these
278 ultrafast time signals.

279

280 **Methods**

281 **Experiments.** The laser source is a homemade Yb-doped mode-locked fiber laser with a spectral
282 width of 0.2 nm. The pulse power is carefully set to strike a balance between strong signals that can
283 be detected by the photodetector and low nonlinear effect suffered by the pulses in the MMF. The
284 large mode area of the 1-km MMF can also help to suppress nonlinear effects³⁹. The step-index core
285 of the MMF can provide much larger intermodal dispersion than a graded-index core⁴⁰. The fiber
286 probe is a triple-cladding fiber with dimensions of 50/70/360 μm (NUFERN FUD-4658, BD-
287 S50/70/360-22FA-HP). The NAs of the core and the second cladding layer of the triple-cladding
288 fiber are 0.2 and 0.46, respectively. The core of the fiber probe approximately matches that of the
289 MMF. The homemade fiber coupler couples light from the source into the second cladding layer of
290 the probe. The fiber-end ball at the end of the probe was made via fusion with a fusion splicer
291 (Fujikura FSM-100P+). Although we adopt a pulse laser, the DMD can perform only grayscale
292 modulation of continuous light, so that all images from the datasets must be binarized before being
293 loaded into the DMD.

294

295 The high-speed camera (MotionBLITZ EoSens® mini) used in the ultrafast experiment has a frame
296 rate of 40 kHz, which is too slow to record the refresh process of the DMD in real time. Thus, the
297 images showing this transient process in Fig. 6(c) were not actually captured during a single refresh
298 process. Instead, they were obtained using the following method. First, we acquired a large number
299 of images while the DMD was periodically switching between the two display images. Because a
300 single refresh process occupies only a very small proportion of a switching period, as shown in Fig.
301 6(b), only a small number of images were captured exactly during the refresh processes. Because
302 these images tended to record different states of the process, they could be combined to represent a
303 continuous refresh process. The exposure time of the camera was set to the minimum to capture
304 these transient states.

305

306 **Training.** The original images were interpolated into 64×64 matrixes as the output, while the 4096-
307 point waveforms were reshaped into 64×64 matrixes as the input to the network. In the data
308 collection stage, for each type of image, 20000 different images of handwritten digits were
309 successively displayed on the DMD, and the corresponding output time signals were collected. In
310 the training stage, the data were divided into 17000 waveform/image pairs as the training set, 2000
311 waveform/image pairs as the validation set and 1000 waveform/image pairs as the test sets. The U-
312 Net model converged after approximately 30 epochs of iteration. Then, the 1000 test waveforms
313 were fed to the trained model to reconstruct the corresponding images. The structure of the U-Net
314 network is shown in Supplementary Note 4.

315

316 **References**

317 1 Feist, A., Silva, N. R. D., Liang, W., Ropers, C. & Schfer, S. Spatio-Temporal Probing of Lattice
318 Dynamics in Graphite by Ultrafast TEM. *European Microscopy Congress 2016: Proceedings*.
319 330-331 (2016).

320 2 El-Desouki *et al.* CMOS Image Sensors for High Speed Applications. *Sensors* (2009).
321 3 Nakagawa, K. Sequentially timed all-optical mapping photography for observation of ultrafast
322 phenomena. *2015 Opto-Electronics and Communications Conference (OECC)*. 15650105
323 (2015).
324 4 Li, Z., Zgadzaj, R., Wang, X., Chang, Y. Y. & Downer, M. C. Single-shot tomographic movies
325 of evolving light-velocity objects. *Nat. Commun.* **5**, 3085 (2014).
326 5 Xiaofang *et al.* High-frame-rate observation of single femtosecond laser pulse propagation in
327 fused silica using an echelon and optical polarigraphy technique. *Appl. Opt.* **53**, 8395-8399
328 (2014).
329 6 Wang, P., Liang, J. & Wang, L. V. Single-shot ultrafast imaging attaining 70 trillion frames per
330 second. *Nat. Commun.* **11**, 2091 (2020).
331 7 Feist, A., Silva, N. R. D., Liang, W., Ropers, C. & Schfer, S. Spatio-Temporal Probing of Lattice
332 Dynamics in Graphite by Ultrafast TEM. *European Microscopy Congress 2016: Proceedings*.
333 (2016).
334 8 Block, A., Liebel, M., Yu, R., Spector, M. & Hulst, N. F. V. Tracking ultrafast hot-electron
335 diffusion in space and time by ultrafast thermomodulation microscopy. *Sci. Adv.* **5**, eaav8965
336 (2019).
337 9 Zyung, T., Kim, H., Postlewaite, J. C. & Dlott, D. D. Ultrafast imaging of 0.532 - μ m laser
338 ablation of polymers: Time evolution of surface damage and blast wave generation. *J. Appl.*
339 *Phys.* **65**, 4548-4563 (1989).
340 10 Gawelda, W. *et al.* Ultrafast imaging of transient electronic plasmas produced in conditions of
341 femtosecond waveguide writing in dielectrics. *Appl. Phys. Lett.* **93**, 231115 (2008).
342 11 Osmanski, B. F. *et al.* Ultrafast imaging of blood flow dynamics in the myocardium. *IEEE Trans.*
343 *Med. Imaging* **31**, 1661-1668 (2012).
344 12 Deffieux, T., Gennisson, J.-L., Tanter, M., Fink, M. & Nordez, A. Ultrafast imaging of in vivo
345 muscle contraction using ultrasound. *Appl. Phys. Lett.* **89**, 184107 (2006).
346 13 Li, Y. *et al.* Deep cytometry: deep learning with real-time inference in cell sorting and flow
347 cytometry. *Sci. Rep.* **9**, 11088 (2019).
348 14 Mehta, A. D., Jung, J. C., Flusberg, B. A. & Schnitzer, M. J. Fiber optic in vivo imaging in the
349 mammalian nervous system. *Curr. Opin. Neurobiol.* **14**, 617-628 (2004).
350 15 Petty, H. R. Spatiotemporal chemical dynamics in living cells: from information trafficking to
351 cell physiology. *Biosystems* **83**, 217-224 (2006).
352 16 Dufour, J., Murat, D., Dufour, X. & Foos, J. Experimental Observation of Nuclear Reactions in
353 Palladium and Uranium—Possible Explanation by Hydrex Mode. *Fusion Sci. Technol.* **40**, 91-
354 106 (2001).
355 17 Rahmani, B., Loterie, D., Konstantinou, G., Psaltis, D. & Moser, C. Multimode optical fiber
356 transmission with a deep learning network. *Light: Science & Applications* **7**, 69 (2018).
357 18 Wu, L. *et al.* Analysis and Design of a CMOS Ultra-High-Speed Burst Mode Imager with In-
358 Situ Storage Topology Featuring In-Pixel CDS Amplification. *Sensors* **18**, 3683 (2018).
359 19 El-Desouki *et al.* CMOS Image Sensors for High Speed Applications. *Sensors* **9**, 430-444
360 (2009).
361 20 Goda, K., Tsia, K. & Jalali, B. Serial time-encoded amplified imaging for real-time observation
362 of fast dynamic phenomena. *Nature* **458**, 1145-1149 (2009).
363 21 Karpf, S. *et al.* Spectro-temporal encoded multiphoton microscopy and fluorescence lifetime

364 imaging at kilohertz frame-rates. *Nat. Commun.* **11**, 2026 (2020).

365 22 Liao, R., Hon, N. K., Buckley, B. W., Diebold, E. D. & Jalali, B. Chromo-modal dispersion for
366 optical communication and time-stretch spectroscopy. *Opt. Lett.* **46**, 500-503 (2021).

367 23 Zhu, C. *et al.* Image reconstruction through a multimode fiber with a simple neural network
368 architecture. *Sci. Rep.* **11**, 896 (2021).

369 24 Mahalati, R. N., Gu, R. Y. & Kahn, J. M. Resolution limits for imaging through multi-mode
370 fiber. *Opt. Express* **21**, 1656-1668 (2013).

371 25 Lee, J. & Kim, D. Determination of the differential mode delay of a multimode fiber using
372 Fourier-domain intermodal interference analysis. *Opt. Express* **14**, 9016-9021 (2006).

373 26 Cheng, J. *et al.* Time-domain multimode dispersion measurement in a higher-order-mode fiber.
374 *Opt. Lett.* **37**, 347-349 (2012).

375 27 Xiao, Q., Yan, P., Ren, H., Chen, X. & Gong, M. A side-pump coupler with refractive index
376 valley configuration for fiber lasers and amplifiers. *J. Lightwave Technol.* **31**, 3015-3022 (2013).

377 28 Deng, L. The mnist database of handwritten digit images for machine learning research [best of
378 the web]. *IEEE Signal Process. Mag.* **29**, 141-142 (2012).

379 29 Borhani, N., Kakkava, E., Moser, C. & Psaltis, D. Learning to see through multimode fibers.
380 *Optica* **5**, 960-966 (2018).

381 30 Li, Y. *et al.* Image Reconstruction Using Pre-Trained Autoencoder on Multimode Fiber Imaging
382 System. *IEEE Photonics Technol. Lett.* **32**, 779-782 (2020).

383 31 Cohen, G., Afshar, S., Tapson, J. & Van Schaik, A. EMNIST: Extending MNIST to handwritten
384 letters. *2017 International Joint Conference on Neural Networks (IJCNN)*. 2921-2926 (2017).

385 32 Xiao, H., Rasul, K. & Vollgraf, R. Fashion-MNIST: a Novel Image Dataset for Benchmarking
386 Machine Learning Algorithms. *arXiv preprint*, cs.LG/1708.07747 (2017).

387 33 Conner, J. L., Overlaur, M. & Bhuva, R. L. Spatial light modulator with buried passive charge
388 storage cell array. US patent 5,671,083 (1997).

389 34 Joshi, A. M., Heine, F. & Feifel, T. Rad-hard ultrafast InGaAs photodiodes for space
390 applications. *Proc. SPIE 6220*. 622003 (2006).

391 35 Atakaramians, S., Afshar, S., Monro, T. M. & Abbott, D. Terahertz dielectric waveguides. *Adv.*
392 *Opt. Photonics* **5**, 169-215 (2013).

393 36 Velten, A. *et al.* Recovering three-dimensional shape around a corner using ultrafast time-of-
394 flight imaging. *Nat. Commun.* **3**, 745 (2012).

395 37 Turpin, A., Musarra, G., Kapitany, V., Tonolini, F. & Faccio, D. Spatial images from temporal
396 data. *Optica* **7**, 900-905 (2020).

397 38 Jalali, B., Jiang, Y. & Karpf, S. Time stretch lidar: a fast spectrally scanned time-of-flight 3D
398 camera. *Proc. SPIE 11684*. 116841B (2021).

399 39 Namihira, Y. ITU-T round robin measurement for nonlinear coefficient (n_2/A_{eff}) of various
400 single mode optical fibers. *Technical Digest: Symposium on Optical Fiber Measurements, 2004*.
401 33-36 (2004).

402 40 Keiser, G. *Wiley encyclopedia of telecommunications* (McGraw Hill, New York, 2000).

403

Supplementary Files

This is a list of supplementary files associated with this preprint. Click to download.

- [SupplementMaterial.pdf](#)
- [SupplementMaterial.pdf](#)